Institut für Energie- und Klimaforschung
Plasmaphysik (IEK-4)

Numerical estimate of the multi-species ion sound speed of Langmuir probe interpretations in edge plasmas of Wendelstein 7-X

J. Cosfeld, M. Rack, D. Reiter, P. Drews, B. Blackwell, M. Jakubowski, H. Niemann, D. Zhang, Y. Feng, and the Wendelstein 7-X Team

Jül-4414

Mitglied der Helmholtz-Gemeinschaft

JÜLICH
Forschungszentrum

Institut für Energie- und Klimaforschung
Plasmaphysik (IEK-4)

Numerical estimate of the multi-species ion sound speed of Langmuir probe interpretations in edge plasmas of Wendelstein 7-X

J. Cosfeld, M. Rack, D. Reiter, P. Drews, B. Blackwell, M. Jakubowski, H. Niemann, D. Zhang, Y. Feng, and the Wendelstein 7-X Team

Berichte des Forschungszentrums Jülich
Jül-4414 · ISSN 0944-2952
Institut für Energie- und Klimaforschung
Plasmaphysik (IEK-4)

Vollständig frei verfügbar über das Publikations-
portal des Forschungszentrums Jülich (JuSER)
unter www.fz-juelich.de/zb/openaccess

Forschungszentrum Jülich GmbH · 52425 Jülich
Zentralbibliothek, Verlag
Tel.: 02461 61-5220 · Fax: 02461 61-6103
zb-publikation@fz-juelich.de
www.fz-juelich.de/zb

Numerical estimate of the multi-species ion sound speed of Langmuir probe interpretations in edge plasmas of Wendelstein 7-X

J. Cosfeld[1], M. Rack[1,2], D. Reiter[1], P. Drews[1], B. Blackwell[3], M. Jakubowski[4], H. Niemann[4], D. Zhang[4], Y. Feng[4], and the Wendelstein 7-X Team

[1]Forschungszentrum Jülich GmbH, Insitut für Energie- und Klimaforschung – Plasmaphysik, Partner of the Trilateral Euregio Cluster (TEC), 52425 Jülich, Germany

[2] JARA-HPC, Jülich Supercomputing Centre, Forschungszentrum Jülich GmbH, 52425 Jülich, Germany

[3]Australian National University, Acton ACT, 2601 Canberra, Australia

[4]Max-Plank-Insitut für Plasmaphysik, 17491 Greifswald / 85748 Garching, Germany

E-mail: `j.cosfeld@fz-juelich.de`

Abstract. The three-dimensional Monte-Carlo transport code package EMC3-EIRENE has been widely applied as edge plasma analysis tool for more than a decade now, resulting in successful validation against various measured trends seen in stellarator and tokamak plasma boundaries. We apply this code package for Wendelstein 7-X (W7-X) discharges in interpretive mode. Today, W7-X plasma discharges still lack diagnostics to directly measure some important edge plasma properties, such as the spatial distribution of the multi species sound speed, which is affected by the effective charge state and the effective mass. Here, EMC3-EIRENE simulations are applied to reconstruct these properties computationally. It can be shown that, earlier assumptions on the effective charge state distribution and the effective mass for reported Langmuir probe measurements have to be revised. Reprocessing of up- and down-stream Langmuir probe measurements with code interpreted spatial profiles of the effective charge state and the effective mass now lead to an overall improved physical consistency.

Keywords: Wendelstein 7-X, plasma-wall interaction, numerical diagnostic, EMC3-EIRENE

1. Introduction

Wendelstein 7-X (W7-X) [1] represents one of the most modern magnetic confinement fusion experiments today. It is based on an optimised stellarator magnetic configuration. W7-X has a modular set of 50 non-planar and 10 planar coils to shape the geometry of the magnetic field in a favorable way [2]. Plasma dynamics within the complex three-dimensional structure of a stellarator can only partially be assessed by the installed diagnostics.

For this purpose the three-dimensional plasma edge code, which is treating complex magnetic field configurations with a fluid Monte-Carlo approach (EMC3) [3] coupled to the kinetic particle transport code EIRENE [4], is utilised in this study. EMC3 solves a set of macroscopic reduced Braginskii conservation equations [5] for the particle, parallel momentum and energy balance, while EIRENE solves multi-species Boltzmann equations of particles with internal states and inelastic collision processes. In order to make connection with the common terminology in numerical analysis [6], we note that for EMC3-EIRENE, non-linear coupling between the various equations and plasma components is carried out conservatively within the identity preserving Lagrangian "particle"-frame (e.g. for electron and ion energy, or for positive and negative ion momentum). In other cases Lagrangian quantities are first projected onto an intermediate (Eulerian) grid, and then re-sampled. EIRENE provides particle, momentum and energy sources and sinks from the kinetically treated components. Classical electron and main ion transport assumption (without kinetic corrections so far) is applied for the parallel heat transport in EMC3, while the perpendicular transport is treated by an anomalous diffusion ansatz. The implementation of light impurities (impurity ions with small atomic number Z) consists of a "trace fluid model" which allows only a small electron density perturbation by each impurity species.

In the first operational campaign W7-X was operated in limiter configuration [7, 8]. Different Langmuir probe diagnostics are installed on the limiter surface [9] and on the probe head of a multi-purpose manipulator (MPM) [10–12]. However, the interpretation of these Langmuir probe measurements require information of the plasma's impurity content which is missing so far. For example diagnostics for the effective charge state distribution Z_{eff} and the effective mass m_{eff} measurements, were not available in the first operational campaign of W7-X. A constant value or a profile of Z_{eff} and m_{eff} are a commonly used quantities for characterizing the global impurity content in the plasma [13].

Figure 1 gives a preliminary overview of the distribution of Z_{eff} in the plasma scenario, assessed by EMC3-EIRENE simulations for a plasma with carbon as only impurity.

A consistency between plasma edge profiles (T_{e} and n_{e}) assessed by EMC3-EIRENE simulations and down-stream Langmuir probe measurements is enforced. Furthermore, a consistency is achieved between EMC3-EIRENE simulations and up-stream Langmuir probe measurements. To our knowledge no attempt, to quantitatively reconstruct Z_{eff} and m_{eff} profiles was made. These simulations are consistent with several diagnostics.

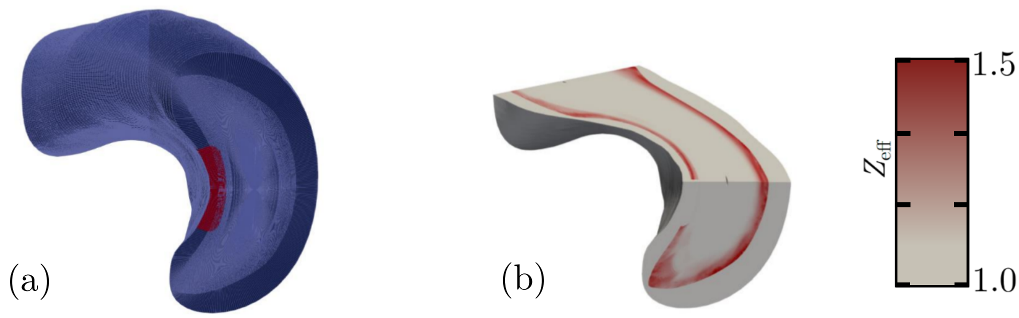

Figure 1: Overview of the computational domain of EMC3 (a) and a schematic two dimensional toroidal plot of Z_{eff}

The deduced profiles can be included in a refinement process of the Langmuir probe measurement interpretations. In the present paper a consistent reconstruction of Z_{eff} for a plasma with carbon as only impurity, via an iterative process between EMC3-EIRENE simulations and refined up-stream measurement data-sets, is achieved. This approach includes convergence criteria for deduced plasma parameters which lead to a final reconstructed charge state Z_{eff} and a final effective mass m_{eff}. By the combination of the comparison- and reconstruction process, EMC3-EIRENE is applied as a three-dimensional interpretation tool for W7-X discharges with carbon impurities.
The structure of this publication is as follows: First, in section 2, an overview of the EMC3-EIRENE model used in this paper will be given. Then, in section 3, the conditioning of EMC3-EIRENE simulations will be discussed. In particular, the beneficial impact of the EMC3-EIRENE simulations on Langmuir probe measurements, resulting in the assessment of internal consistency between different Langmuir probe data-sets, is investigated. The iterative process used to reconstruct the effective charge state and the effective mass is motivated, described and discussed in section 4. Main results are summarized in the conclusion.

2. EMC3-EIRENE

In the EMC3-EIRENE Monte-Carlo code package, a three-dimensional edge plasma transport model with a self-consistent iterative treatment of the plasma and neutral gas phases [4, 14–16] is implemented. EMC3 solves a set of three-dimensional fluid equations in an externally given magnetic field geometry. A detailed derivation of the EMC3 model equations can be found in [3]. Balance equations are solved for the quasi-neutral ($n_{\text{e}} = n_{\text{i}} = n$) plasma density n, the parallel velocity $u_{\parallel}$, and temperature T_{α} (with $\alpha \in \{\text{e}, \text{i}\}$) of single ion component plasma particles. They read, respectively:

$$\boldsymbol{\nabla} \cdot \left[n u_{\parallel} \hat{\mathbf{e}}_{\parallel} - D_{\perp} \boldsymbol{\nabla}_{\perp} n \right] = S_{\text{i}} \quad , \tag{1}$$

$$\boldsymbol{\nabla} \cdot \left[m_{\text{i}} n u_{\parallel} u_{\parallel} \hat{\mathbf{e}}_{\parallel} - \eta_{\parallel} \boldsymbol{\nabla}_{\parallel} u_{\parallel} - D_{\perp} \boldsymbol{\nabla}_{\perp} \left(m_{\text{i}} n u_{\parallel} \right) \right] = -\hat{\mathbf{e}}_{\parallel} \cdot \boldsymbol{\nabla} p + S_{\text{m}} \quad , \tag{2}$$

$$\nabla \cdot \left[\frac{5}{2} n T_\alpha u_\parallel \hat{\mathbf{e}}_\parallel - \kappa_{\alpha\parallel} \nabla_\parallel T_\alpha - \frac{5}{2} T_\alpha D_\perp \nabla_\perp n - \chi_{\alpha,\perp} n \nabla_\perp T_\alpha \right] \tag{3}$$
$$= \xi \frac{3 m_\mathrm{e} n_\mathrm{e}}{m_\mathrm{i} \tau_\mathrm{ee}} (T_\mathrm{e} - T_\mathrm{i}) + S_{\mathrm{e},\alpha} - \delta_{\alpha\mathrm{e}} S_{\mathrm{e,cool}} \quad , \quad \xi = \begin{cases} +1 \ , \ \text{for } \alpha = \mathrm{i} \\ -1 \ , \ \text{for } \alpha = \mathrm{e} \end{cases}$$

where $\hat{\mathbf{e}}_\parallel$ is the unit vector in direction of the magnetic field, m_α represents the mass of the particle type α and τ_ee is the mean collision time between two electrons. The total plasma pressure p equals the sum of the electron plus ion temperature T_α times the density n: $p = n(T_\mathrm{e} + T_\mathrm{i})$. All EMC3 model equations are based on the plasma transport theory from Braginskii [5] with classical parallel transport coefficients $\eta_\parallel, \kappa_{\alpha,\parallel}$. The anomalous cross-field transport is taken into account by free model diffusion parameters $D_\perp$ and $\chi_{\mathrm{e,i}\perp}$.

The (also anomalous) perpendicular viscosity $\eta_\perp$ is re-expressed via combining the perpendicular components of the convective $(\nabla \cdot [m_\mathrm{i} n V_{\mathrm{i}\parallel} \boldsymbol{V}_{\mathrm{i}\perp}])$ and viscous stress $\nabla \cdot [\eta_\perp \underline{\mathbf{I}}_\perp \cdot \nabla V_{\mathrm{i}\parallel}]$ terms, using the perpendicular particle diffusion ansatz: $n\boldsymbol{V}_{\mathrm{i}\perp} = -D_\perp \nabla_\perp n$. This yield the third term on the l.h.s. in equation (2), when furthermore the viscosity coefficient $\eta_\perp$ for viscous momentum fluxes due to perpendicular gradients in $V_\parallel$ is fixed by the ansatz $\eta_\perp = n m_\mathrm{i} D_\perp$ [16].

Interactions between neutrals, plasma electrons and ions are treated by the source terms S_i, S_m, and $S_{\mathrm{e},\alpha}$, which are obtained from the EIRENE code. Impurities released from plasma facing wall components cool the electrons via the energy sink $S_\mathrm{e,cool}$ appearing only in the electron energy balance. The attenuation effects due to impurity ions are still neglected, i.e. $n_\mathrm{e} = n_\mathrm{i}$, with the main ions i only. In the post processing, an a posteriori approach was used to consider each ionisation state contribution of carbon to the electron density $n_\mathrm{e} = n_\mathrm{H} + \sum_{Z=1}^{6} Z n_\mathrm{C}^{Z+}$. On average, this increased the electron density by 11% for the considered plasma scenario. A "trace fluid model" is implemented for the description of the impurities, which is limited to small density disturbance [3]. Only a strongly reduced parallel force balance model is used, rather than a full transport equation of the form of equation (2) supplemented by electric, frictional and thermal forces (which have been canceled out between electrons and main plasma ions in equation (2)). A detailed discussion on the implementation of impurities into the edge modeling structure is given in the appendix.

For this work, the five fold periodicity and the up-down stellarator symmetry [1] is taken into account. Therefore, the EMC3-EIRENE simulation grid in this work covers a toroidal segment of $\Delta\varphi_\mathrm{tor} = 36° = 72 \cdot \delta\varphi_\mathrm{tor}$ (with $\delta\varphi_\mathrm{tor}$ denoting the toroidal discretisation) with a resolution of $\Delta R = 0.44$ cm in radial direction, a poloidal grid for each of the 72 poloidal cross-sections (with a poloidal discretisation of $\delta\theta_\mathrm{pol} = 0.7°$). EMC3-EIRENE simulation are carried out on this grid to assess the plasma edge dynamics with a full three-dimensional resolution.

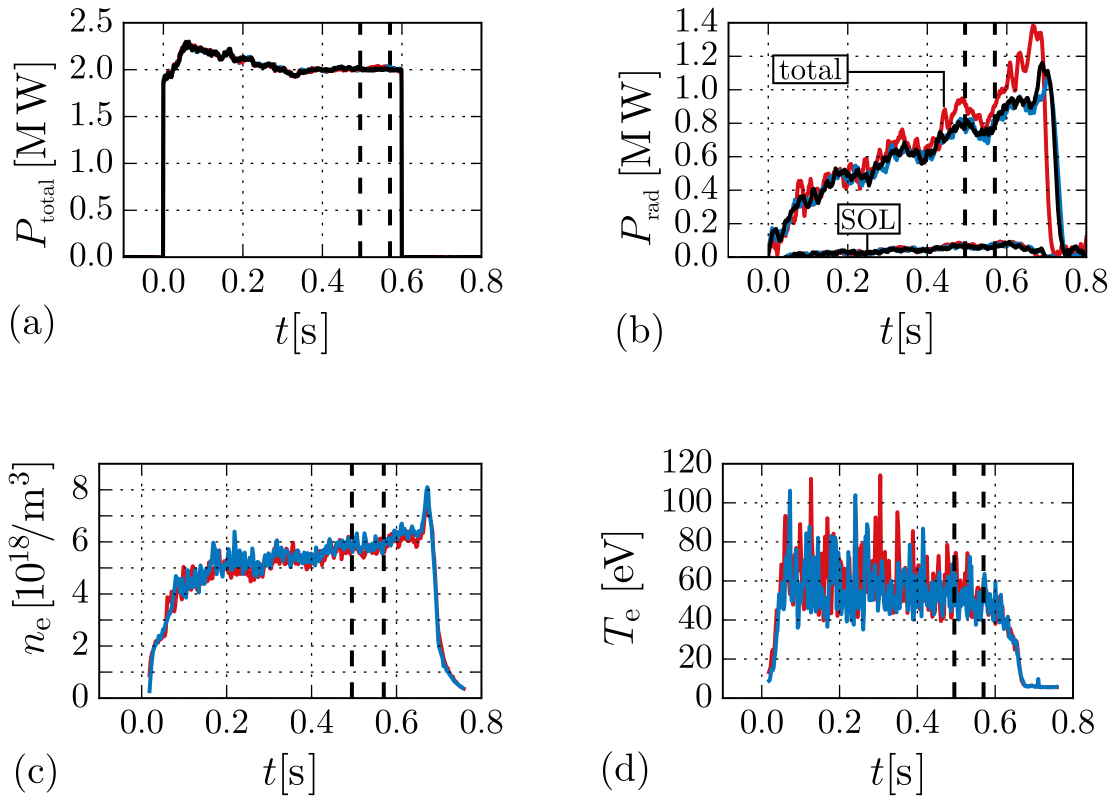

Figure 2: Overview of guiding measurements of heating power (a), radiated power (b), and down-stream n_{e} (c), T_{e} (d). Measurements ((a)-(d)) are carried out by bolometer and Langmuir probe measurements of a repetitive set of W7-X discharges. Color code refers to different discharges. Black: discharge 20160308.22, red: discharge 20160308.23 and blue: discharge 20160308.24. Up-stream Langmuir probe measurements were performed in a specific time interval Δt, indicated by vertical dashed lines.

3. Constraining the EMC3-EIRENE simulations

In the following, we consider EMC3-EIRENE simulations in combination with down-stream Langmuir probe measurements [9]. The varied free simulation parameters are transport coefficients $D_{\perp} = 3\chi_{\text{e},\perp} = 3\chi_{\text{i},\perp}$, the input heating power entering the scrape-off layer (SOL) $P_{\text{heat}}^{\text{SOL}}$, the power radiated in the SOL $P_{\text{rad}}^{\text{SOL}}$, and the density n_{e} at the seperatrix. These free parameters are chosen to match the plasma scenario described in figure 2. The bolometric measurement of P_{rad} gives a measure for the power which is radiated in total $P_{\text{rad}}^{\text{total}}$ and which fraction is radiated in the scrape-off layer $P_{\text{rad}}^{\text{SOL}}$. The simulation requires the heating power entering the SOL as an input parameter. Therefore, power which is lost in the SOL needs to be subtracted from the overall lost power to account for the power loss in the core region (not simulated here). Considered discharges were selected because mid-plane measurements are only available for a small

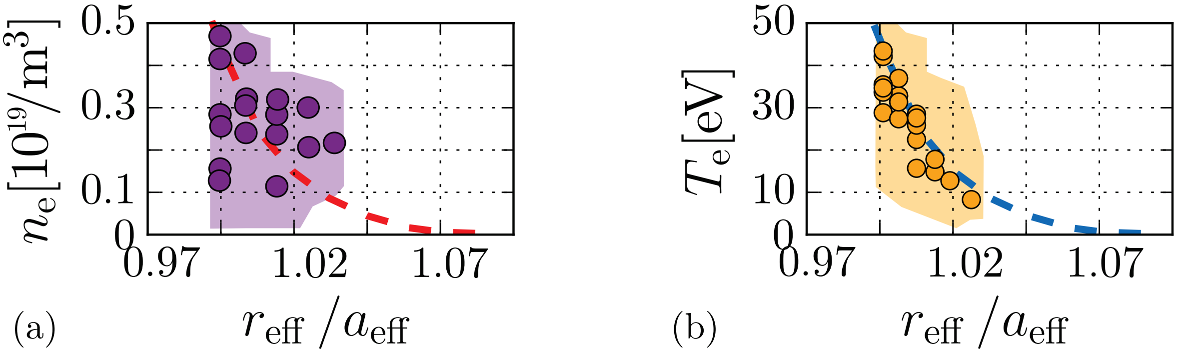

Figure 3: Down-stream comparison of density n_e (a) and temperature T_e (b) of EMC3-EIRENE simulation (dashed) and limiter Langmuir probe measurements (dots, uncertainties of the measurements lie within the shaded region) plotted over the effective radius r_{eff}. The effective radius r_{eff} is calculated via the mean radius of the complete experiment. With a_{eff} characterizing the position of the last closed flux-surface (LCFS). Simulation parameters: $P^{SOL}_{heat} = 1.32$ MW, $P^{SOL}_{rad} = 120$ kW, $n_e^{LCFS} = 6 \times 10^{18}$ m^{-3}, $T_e^{LCFS} = 50$ eV, $D_\perp = 0.5$ m^2/s and $\chi_{e,i\perp} = 3D_\perp$. We refer to this simulation setup as Λ.

sub-set of discharges. A multi-purpose manipulator (MPM) plunged into the plasma over a time interval $\Delta t = 0.05$ s during the discharge time (see figure 2 dashed black lines). Resulting plasma parameters during the plunge time interval are used as input parameters for EMC3-EIRENE simulations. An overall heating power of 2 MW was applied of which in total 0.8 MW were radiated and thereby lost [17]. Considering all possible power losses, this adds up to an heating power entering the scrape-off layer of $P^{SOL}_{heat} = 1.32$ MW and a radiated power in the SOL of $P^{SOL}_{rad} = 120$ kW. By averaging the other measured plasma parameters over Δt one obtains, $n_e^{LCFS} = 6 \times 10^{18}$ m^{-3} and $T_e^{LCFS} = 50$ eV (measured down-stream) which constrain the remaining free simulation parameters. From now on, Λ will refer to this simulation setup. In addition to what is presented in figure 2, the limiter Langmuir probes are spatially resolved in radial direction. Therefore, a comparison between simulations and measurements allows a detailed discussion of radial profiles of n_e and T_e in comparison to up- and down-stream measurements [10]. A comparison of the plasma edge profiles from EMC3-EIRENE simulations to the experimental data-sets resulted in a generally overall agreement and consistency on the down-stream measurement location (see figure 3) and on the up-stream measurement location (see figure 4). But, a small offset between $n_{e,MPM}$ and $n_{e,EMC3}$ remains for the radial most outer measuring points of the MPM (see figure 4). Down-stream Langmuir probe measurements need to be treated with caution as these measurements were performed with eroded probe heads. Thus, only a trend of these measurements can be compared to the EMC3-EIRENE results. The trend of n_e and T_e

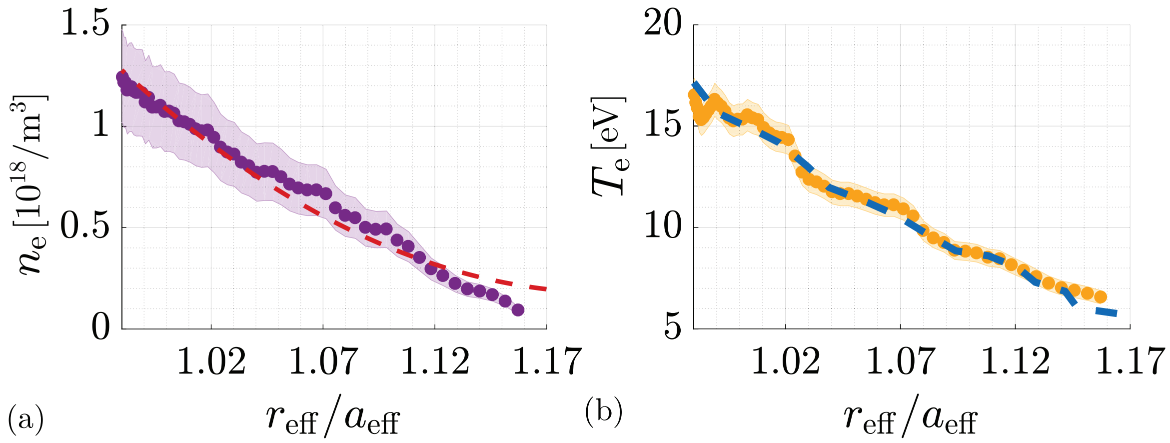

Figure 4: Up-stream comparison of density n_e (a) and temperature T_e (b) of EMC3-EIRENE simulation (dashed) and manipulator Langmuir probe measurements (dots, uncertainties of the measurements shown in the shaded region) plotted over the effective radius r_{eff}. Simulation parameters from Λ.

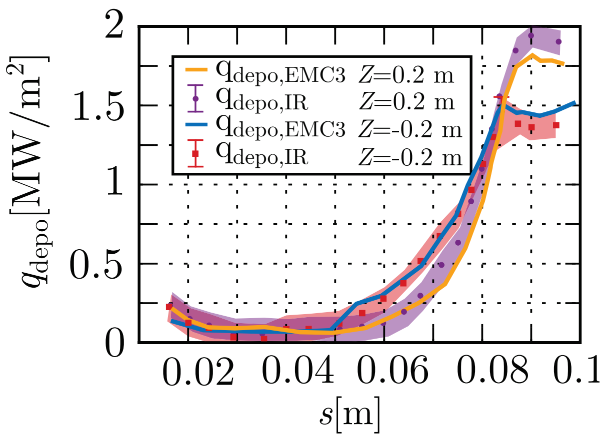

Figure 5: Comparison between EMC3-EIRENE simulation (solid) and heat flux measurements (dots) and their uncertainties (shaded region) plotted against the surface coordinate s of the limiter. See reference plot in [18]. Simulation parameters from Λ.

shows also, aside from the up-stream results, an agreement to EMC3-EIRENE results (see figure 3).

Furthermore, the limiter heat flux measurements [18,19] provide a third reference point for further constraining EMC3-EIRENE simulations. Here, radial heat flux profiles along the limiter at a height Z of 0.2 m and -0.2 m are discussed. Figure 5 shows heat-flux profiles along the surface of the limiter plotted against surface coordinate s. The surface coordinate s is measured along the surface of the limiter away from the limiter tip $s = 0$. The radial heat flux profiles of the measurement are also consistent to EMC3-EIRENE simulation results of Λ.

4. 3D spatially resolved effective charge state and effective mass reconstruction

In this section we discuss reinterpretation of Langmuir probe measurements. The calculation of the electron density from the saturation current I_{sat} (used in the data interpretation process in [10]) measured by the Langmuir probes, is affected by a change of the ion speed of sound c_{s}.

$$n_{\mathrm{e,MPM}} = \frac{I_{\mathrm{sat}}}{0.49 A_{\mathrm{eff}} c_{\mathrm{s}}} \quad . \tag{4}$$

With A_{eff} the effective area of the Langmuir pins. Stangeby [20] defines the speed of sound c_{s} of a single species plasma scenario as,

$$c_{\mathrm{s}}^{\mathrm{single}} = \sqrt{\frac{T_{\mathrm{i}} + Z T_{\mathrm{e}}}{m_{\mathrm{i}}}} \quad . \tag{5}$$

The ion mass is denoted with m_{i}. Stangeby assumes the plasma flow to be isothermal. The adiabatic index $\gamma = 1$ was already applied for equation (5). Plasma temperatures are given in eV, hence the Boltzmann constant k is not introduced in equation (5). Equation (5) is often used to describe plasma scenarios which have carbon or oxygen as second plasma species, aside from hydrogen. Then, $Z = 1$ and $m_{\mathrm{i}} = 1$ are assumed. Presented measurement data-sets from figure 3 and 4 rely on these assumption. The following discussion will put a question to the validity of $Z = 1$ and $m_{\mathrm{i}} = 1$. An expression for the overall plasma speed of sound c_{s} for a multi species plasma was found by Tokar [21],

$$c_{\mathrm{s}}^{\mathrm{multi}} = \sqrt{\frac{\sum_{i=0}^{\kappa} \Gamma_i (T_i + Z_i T_{\mathrm{e}})}{\sum_{i=0}^{\kappa} \Gamma_i m_i}} \quad , \quad \Gamma_i = n_i u_i \quad . \tag{6}$$

The adiabatic index is again set to $\gamma = 1$ and k drops out because of the previously selected units for the plasma temperatures. Furthermore, u_i represents the velocity of one plasma species out of κ plasma species. Hence, u_i is a contribution to the specific plasma species flow Γ_i.

A calculation of $c_{\mathrm{s}}^{\mathrm{multi}}$ for a plasma containing fully ionized carbon impurities results in quite sophisticated algebra. Hence, other studies on the transition between a single species plasma scenario to a multi species plasma scenario introduce the idea to use the effective charge state distribution Z_{eff}, as a "short-cut“, on a single species description [22, 23]. The calculation of an individual ion speed of sound for each plasma species is avoided. So, Z_{eff} becomes an approximation of the sum over all charge states i in the multi species plasma and converts the multi species plasma scenario to an contaminated single species plasma. The same goes for m_{eff}. We use the effective charge state $Z_{\mathrm{eff}} = \sum_i n_i Z_i^2 / \sum_i n_i Z_i$ and effective mass $m_{\mathrm{eff}} = \sum_i n_i m_i / \sum_i n_i$ profiles

in the following to extract information for the reprocessing of the measurement analysis of e.g. Langmuir probes. The code package EMC3-EIRENE provides densities for the main plasma and for every charge state of the considered plasma impuritiy (under the mentioned assumptions). One can easily deduce the local charge state Z_{eff} and the local effective mass m_{eff}. An a posteriori approach was used to consider the effect of the impurities on the electron density for compensating the limitations of the EMC3 impurity model.
Following the fact that Z_{eff} and m_{eff} profiles were not directly measurable during the limiter campaign [1, 8], an assumption of Z_{eff} and m_{eff} along the Langmuir probe measurement location had to be made. The main plasma is here contaminated by a single impurity species like carbon or oxygen. We substitute Z for Z_{eff} and m_{i} for m_{eff} in equation (5) to follow this introduced transition.

$$c_{\mathrm{s}}^{\mathrm{single}} = \sqrt{\frac{T_{\mathrm{i}} + ZT_{\mathrm{e}}}{m_{\mathrm{i}}}} \quad \xrightarrow[m\to m_{\mathrm{eff}}]{Z\to Z_{\mathrm{eff}}} \quad c_{\mathrm{s}}^{\mathrm{single}^*} = \sqrt{\frac{T_{\mathrm{i}} + Z_{\mathrm{eff}}T_{\mathrm{e}}}{m_{\mathrm{eff}}}} \tag{7}$$

The effective mass over all plasma species is calculated via,

$$m_{\mathrm{eff}} = \frac{\sum_{i=0}^{\kappa} n_i m_i}{\sum_{i=0}^{\kappa} n_i} \quad . \tag{8}$$

We continue to insert Z_{eff} and m_{eff} in equation (7) ,

$$\left(c_{\mathrm{s}}^{\mathrm{single}^*}\right)^2 = \left(T_{\mathrm{i}} + \frac{\sum_{i=0}^{\kappa} n_i Z_i^2}{\sum_{i=0}^{\kappa} n_i Z_i} T_{\mathrm{e}}\right) \cdot \left(\frac{\sum_{i=0}^{\kappa} n_i}{\sum_{i=0}^{\kappa} n_i m_i}\right) \quad . \tag{9}$$

Multiplying both factors and identifying a common denominator leads to,

$$\left(c_{\mathrm{s}}^{\mathrm{single}^*}\right)^2 = \frac{\sum_{i=0}^{\kappa} n_i \sum_{i=0}^{\kappa} n_i Z_i T_{\mathrm{i}} + \overbrace{\sum_{i=0}^{\kappa} n_i Z_i^2 \sum_{i=0}^{\kappa} n_i}^{\approx\left(\sum_{i=0}^{\kappa} n_i Z_i\right)^2} T_{\mathrm{e}}}{\sum_{i=0}^{\kappa} n_i m_i \sum_{i=0}^{\kappa} n_i Z_i} \tag{10}$$

$$\approx \frac{\sum_{i=0}^{\kappa} n_i \cancel{\sum_{i=0}^{\kappa} n_i Z_i} T_{\mathrm{i}} + \left(\sum_{i=0}^{\kappa} n_i Z_i\right)^{\cancel{2}} T_{\mathrm{e}}}{\sum_{i=0}^{\kappa} n_i m_i \cancel{\sum_{i=0}^{\kappa} n_i Z_i}} \quad . \tag{11}$$

We assume for the last step, that all plasma species velocities u_i do have the same velocity u and that the ion temperature T_{i} is equal for every plasma species ion temperature T_i,

$$\left(c_{\mathrm{s}}^{\mathrm{single}^*}\right)^2 = \frac{\sum_{i=0}^{\kappa} n_i T_{\mathrm{i}} + \sum_{i=0}^{\kappa} n_i Z_i T_{\mathrm{e}}}{\sum_{i=0}^{\kappa} n_i m_i} \quad \overset{u_i=u\ \forall\ i}{\underset{T_{\mathrm{i}}=T_i\ \forall\ i}{=}} \quad \frac{\sum_{i=0}^{\kappa} u n_i T_i + \sum_{i=0}^{\kappa} u n_i Z_i T_{\mathrm{e}}}{\sum_{i=0}^{\kappa} u n_i m_i} \tag{12}$$

$$\overset{\Gamma_i = u n_i}{=} \quad \frac{\sum_{i=0}^{\kappa} \Gamma_i (T_i + Z_i T_{\mathrm{e}})}{\sum_{i=0}^{\kappa} \Gamma_i m_i} = \left(c_{\mathrm{s}}^{\mathrm{multi}}\right)^2 \quad . \tag{13}$$

In equation (10), an odd assumption, lets call it Ω,

$$\sum_{i=0}^{\kappa} n_i Z_i^2 \sum_{i=0}^{\kappa} n_i \approx \left(\sum_{i=0}^{\kappa} n_i Z_i\right)^2 \quad , \tag{14}$$

was used to make the transition from $c_{\mathrm{s}}^{\mathrm{single}}$ over $c_{\mathrm{s}}^{\mathrm{single}*}$ to $c_{\mathrm{s}}^{\mathrm{multi}}$. Hence, the introduction of Z_{eff} and m_{eff} for (5) can only be applied if Ω is true. To quantify the extent of the uncertainty which is made by introducing Ω, we calculate the difference $\Omega_{12} \equiv \Omega_1 - \Omega_2$ between $\Omega_1 \equiv \sum_{i=0}^{\kappa} n_i Z_i^2 \sum_{i=0}^{\kappa} n_i$ and $\Omega_2 \equiv (\sum_{i=0}^{\kappa} n_i Z_i)^2$. We rewrite the series to obtain two double series expressions of Ω_1 and Ω_2,

$$\Omega_1 = \sum_{j=0}^{\kappa} \sum_{i=0}^{\kappa} n_j Z_j^2 n_i \quad , \quad \Omega_2 = \sum_{j=0}^{\kappa} \sum_{i=0}^{\kappa} n_j Z_j n_i Z_i \quad . \tag{15}$$

The series indices j and i are again representing $\kappa+1$ plasma species. Now, the difference Ω_{12} reads as,

$$\Omega_{12} = \sum_{j=0}^{\kappa} \sum_{i=0}^{\kappa} n_j Z_j^2 n_i - \sum_{j=0}^{\kappa} \sum_{i=0}^{\kappa} n_j Z_j n_i Z_i \tag{16}$$

$$= \sum_{j=0}^{\kappa} \sum_{i=0}^{\kappa} (n_j Z_j^2 n_i - n_j Z_j n_i Z_i) \quad . \tag{17}$$

Terms with $i = j$ cancel out in equation (17). Ω_{12} by the usage of the Kronecker delta. Now, Ω_{12} equals zero if $i = j$. We obtained, with the extraction of the main plasma component ($i = 0$ and $j = 0$) out of Ω_{12} and the previously mentioned assumption, that the considered plasma scenario only holds a second plasma species (impurity) to the main hydrogen plasma ($Z_0 = 1$),

$$\Omega_{12} = \sum_{i=1}^{\kappa} n_0 n_i (1 - Z_i) + \sum_{j=1}^{\kappa} n_0 Z_j n_j (Z_j - 1) + \sum_{j=1}^{\kappa} \sum_{i=1}^{\kappa} (n_j Z_j n_i (Z_j - Z_i)) \quad . \tag{18}$$

Each series starting from $j = 1$ and $i = 1$ describe the charge states from the second impurity plasma species. Hence, $Z_i = i$ and $Z_j = j$ can be used to further simplify equation (18),

$$\Omega_{12} = \sum_{i=1}^{\kappa} n_0 n_i (1 - i) + \sum_{j=1}^{\kappa} n_0 j n_j (j - 1) + \sum_{j=1}^{\kappa} \sum_{i=1}^{\kappa} n_j j n_i (j - i) \quad . \tag{19}$$

The uncertainty Ω_{12} can then be calculated via equation (19). We proceed with the same algebra for Ω_2 to find,

$$\Omega_2 = \sum_{i=1}^{\kappa} n_0 n_i i + \sum_{j=1}^{\kappa} n_0 n_j j + \sum_{j=1}^{\kappa} \sum_{j=1}^{\kappa} n_j j n_i i \quad . \tag{20}$$

(a)

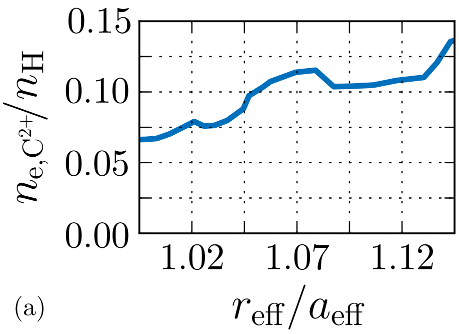

(b)

plasma species	charge state i,j	maximum of individual density
1	0	n_H
2	0	0
	1	$0.05 n_H$
	2	$0.15 n_H$
	3	$0.08 n_H$
	4	$0.01 n_H$
	5	$0.005 n_H$
2	6	$0.004 n_H$

(c)

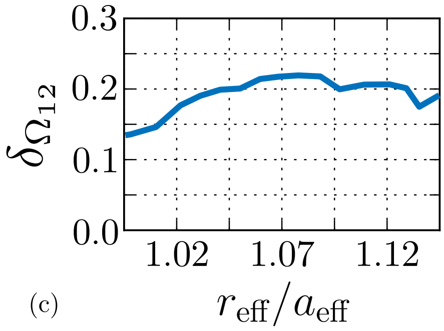

Figure 6: (a) Maximum density $n_{\mathrm{e,C^{2+}}}$ of the impurity plasma species (carbon for the considered plasma scenario) plotted against r_{eff}. (b) Chart of each maximum individual charge state density of hydrogen and carbon. (c) $\delta_{\Omega_{12}}$ profile calculated via profiles shown in chart (b). Simulation results are taken from simulation Λ.

Equation (19) and equation (20) are then used to obtain the uncertainty Ω_{12} in percent,

$$\delta_{\Omega_{12}} = \frac{\Omega_{12}}{\Omega_2} \quad . \tag{21}$$

The maximum density contributions from the plasma scenario Λ (see chart in figure 6) and equation (21) can be used to give a first simple error estimation. Assumption Ω leads to a maximum uncertainty of 21.39% for the considered plasma scenario Λ. Thereby, the shown simplification of a multi species description for plasma $c_{\mathrm{s}}^{\mathrm{multi}}$ to a single species description, including the effective charge state - and mass, $c_{\mathrm{s}}^{\mathrm{single*}}$ has a peak uncertainty of 21.39%. Further, values of chart (b) in shown in figure 6 can then also be used to calculate the overall uncertainty $\delta_{c_{\mathrm{s}}^{\mathrm{multi}}}$ for equation (7) which is introduced via assumption Ω. We use T_{e} and T_{i} from the EMC3-EIRENE simulation (peak values) of plasma scenario Λ and find $\delta_{c_{\mathrm{s}}^{\mathrm{multi}}}$ to be at a maximum of 7.67%. We can use equation (7) to describe a multi species plasma, since a maximum uncertainty $\delta_{\Omega_{12}} = 21.39\%$ leading to $\delta_{c_{\mathrm{s}}^{\mathrm{multi}}} = 8\%$ for plasma scenario Λ is acceptable. The simulation using the setup Λ clearly shows that these assumptions, $Z_{\mathrm{eff}} = 1$ and $m_{\mathrm{eff}} = 1$, are not valid (see figure 7 (a)-(d)). Hence, a recalibration of the measurements (see figure 8), using the presumably more plausible Z_{eff} and m_{eff} profiles shown in figure 7, is required.

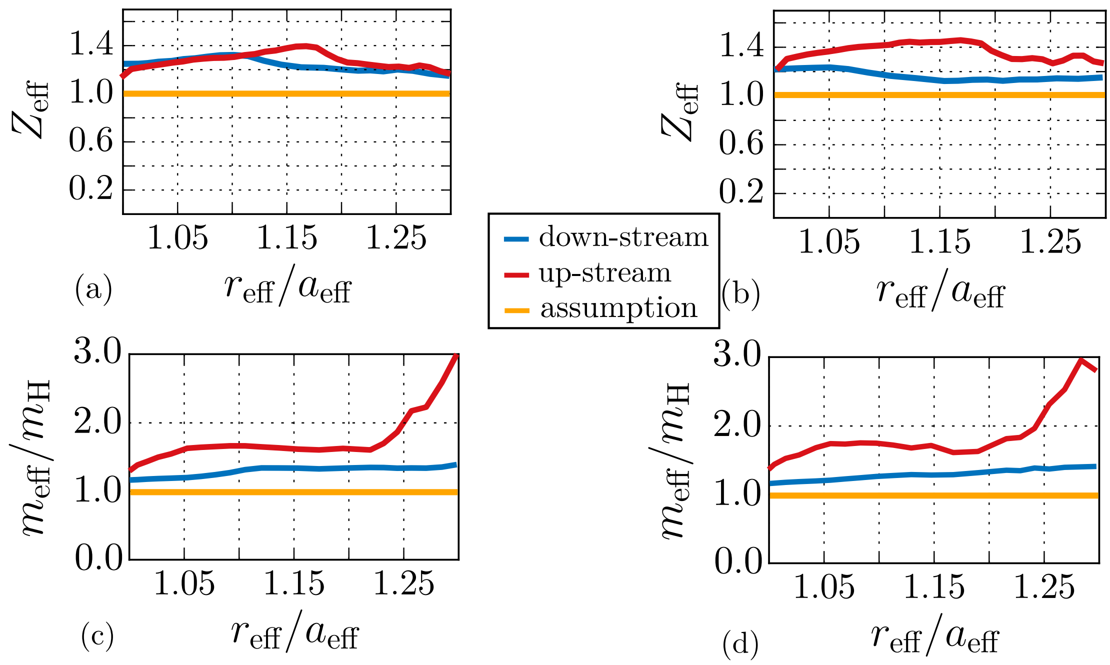

Figure 7: Comparison of the simulated Z_{eff} (top row) and m_{eff} (bottom row), at the down- (blue) and up-stream (red) measurement location, to the previously made assumption $Z_{\mathrm{eff}} = 1$ and $m_{\mathrm{eff}} = 1$ (yellow). All results are plotted against the effective radius r_{eff} normalized to a_{eff}. Subplots (a) and (c) show the results of simulation $\Lambda^{l=1}$, subplots (b) and (d) show the results of the simulation $\Lambda^{l_{\mathrm{end}}}$.

Obviously, this needs to be followed by an adjustment of the simulation as at least one of the constrains changed, visual by the offset between $n_{\mathrm{e,EMC3}}$ and $n_{\mathrm{e,MPM}}$ (see figure 8). The discussed constraining in section 3, with the purpose to match measurements with EMC3-ERIENE simulations, needs to be redone. For this reason, an iterative process is used from this set of EMC3-EIRENE simulations, where each simulation refers to an iterative step l. The simulation setups are now reaching from $\Lambda = \Lambda^{l=1}$ to $\Lambda^{l_{\mathrm{end}}}$. Z_{eff} and m_{eff} profiles will be deduced from the simulations in each iterative step l and will be used for a recalibration of the measurement. A schematic overview of the first iterative step is shown in figure 8, each sub-figure (reaching from (a) to (d)) is corresponding to the sub-steps of the first iterative step. The schematic overview discusses the iterative process for the up-stream multi-purpose manipulator (MPM) measurements. It should be noted that the iterative process is also applied to down-stream Langmuir probe measurements. Density profiles measured by the MPM (up-stream) are used as reference in figure 8. The first iterative step begins with the assessment of $Z_{\mathrm{eff}}^{l=1}$ (sub-step (a) and (b), see figure 8) from the n_{e} profiles shown in figure 4. In the next sub-step (c) of figure 8, an updated $n_{\mathrm{e,MPM}}^{\Lambda^{l=1}}$ profile including the assessed $Z_{\mathrm{eff}}^{l,\mathrm{up-stream}}$ and $m_{\mathrm{eff}}^{l,\mathrm{up-stream}}$ profile is shown. Hence, one can note a displacement regarding $n_{\mathrm{e,MPM}}^{l=1}$ in a comparison of sub-step

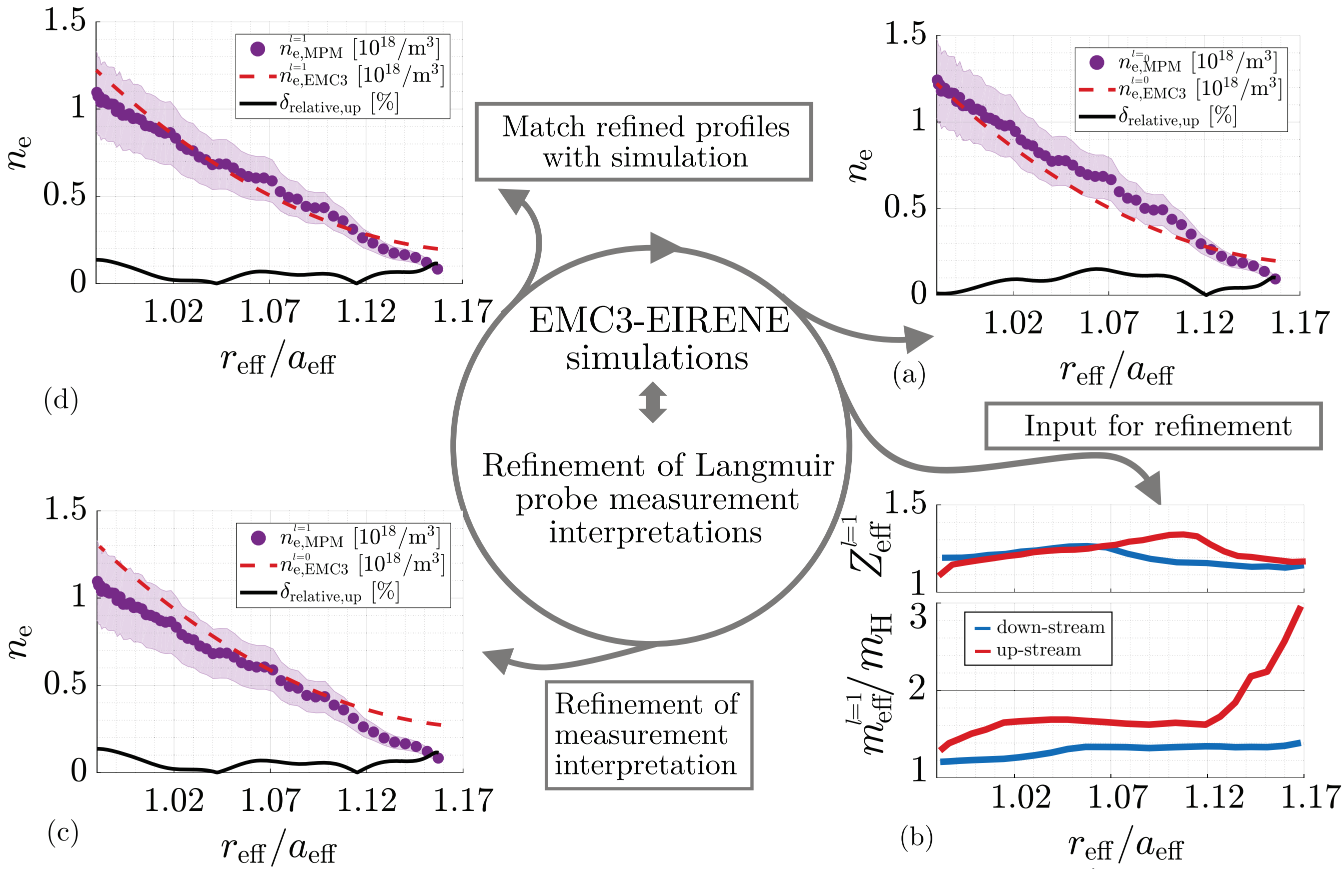

Figure 8: Schematic overview of the first step $l = 1$ of the iterative process. Electron density from Λ (a), $Z_{\text{eff}} = 1$ and $m_{\text{eff}} = 1$ was assumed for $n_{\text{e,MPM}}$. Deduced Z^l_{eff} and m^l_{eff} profiles (b). Relative deviation $\delta^l_{\text{relative,up}}$ (see equation (22)) plotted in the comparison plot of the numeric and measured density data-set(c) and (d). The rework of plot 4 is shown in (d).

(a) and sub-step (c) shown in figure 8. This introduced displacement of $n^{l=1}_{\text{e,MPM}}$ has to be matched with input parameters of EMC3-EIRENE. The input up-stream density is then changed, since we take the up-stream measurements as . For sub-step (d), a switch from an input density (discussed in chapter 2) of $n_{\text{e}} = 3 \times 10^{18}\ \text{m}^{-3}$ to $2.853 \times 10^{18}\ \text{m}^{-3}$ was applied to match $n^{l=1}_{\text{e,MPM}}$ of sub-step (c) with $n^{l=1}_{\text{e,EMC3}}$. The first iterative step is completed, since the consistency between $n^{l=1}_{\text{e,MPM}}$ and $n^{l=1}_{\text{e,EMC3}}$ is again achieved. The relative deviation of the EMC3-EIRENE density profile $n^{l}_{\text{e,EMC3}}$ and $n^{l}_{\text{e,MPM}}$ is calculated via,

$$\delta^{l=1}_{\text{relative,up}} = \text{mean}\left(\frac{n^{l=1}_{\text{e,EMC3}} - n^{l=1}_{\text{e,MPM}}}{n^{l=1}_{\text{e,EMC3}}}\right) \quad . \tag{22}$$

This measure is used to quantify the convergence of the density profiles to each other. Subsequently, the next iteration steps are carried out following the same scheme of sub-steps as shown and discussed in figure 8. The appropriate factor ε^l for a recalibration of the input up-stream density n_{e} of the simulation for the iterative step $l + 1$ can be

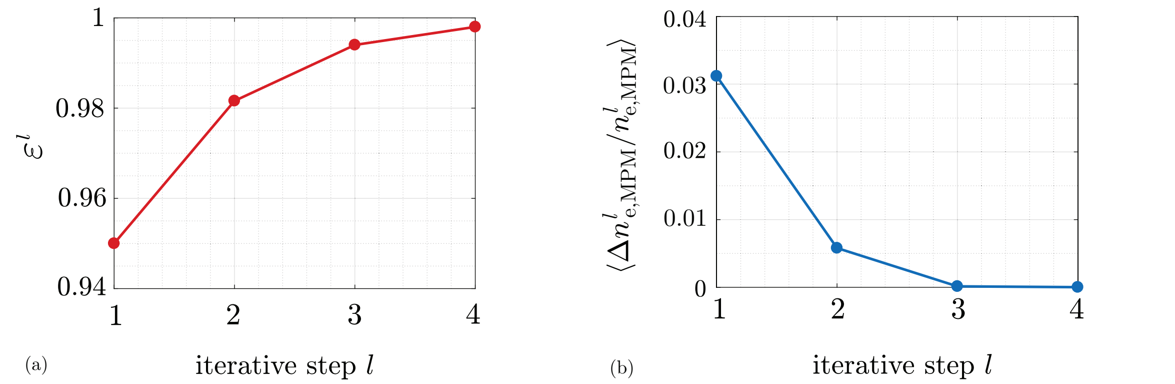

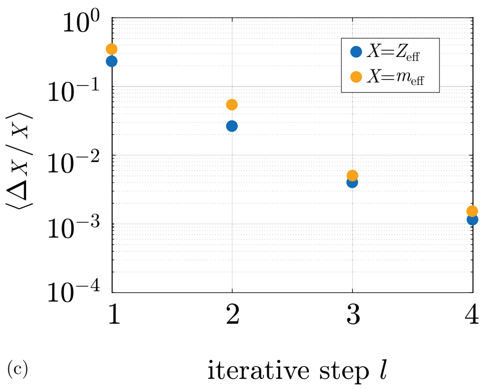

step l	input density [$\mathrm{m}^3/10^{18}$]	ε^l	$\langle \Delta Z_{\mathrm{eff}} / Z_{\mathrm{eff}} \rangle$	$\langle \Delta m_{\mathrm{eff}} / m_{\mathrm{eff}} \rangle$	$\langle \Delta n^l_{\mathrm{e,MPM}} / n^l_{\mathrm{e,MPM}} \rangle$
1	3	0.951	0.23	0.25	0.31
2	2.853	0.982	0.026	0.036	0.005
3	2.801	0.992	0.009	0.014	0.003
4	2.793	0.997	0.003	0.005	0.001

(d)

Figure 9: Factor ε^l plotted against each iteration step (a). The relative change of the the refined MPM measurement of $n^l_{\mathrm{e,MPM}}$ plotted against each iteration step (b). The relative change of the Z_{eff} and m_{eff} profiles is plotted against each iteration step in (c). Simulation parameters are taken from plasma scenario Λ, but n_e was iterated from 3×10^{18} m^{-3} down to 2.793×10^{18} m^{-3}. Chart (d) shows the exact values of each iterative step.

quantified by (using equation (4) and the right hand side of (7)),

$$\varepsilon^l(r) = \frac{n^l_{\mathrm{e,MPM}}(r)}{n^{l-1}_{\mathrm{e,MPM}}(r)} = \sqrt{\frac{T^{l-1}_{\mathrm{i}}(r) + Z^{l-1}_{\mathrm{eff}}(r) T^{l-1}_{\mathrm{e}}(r)}{m^{l-1}_{\mathrm{eff}}(r)} \cdot \frac{m^l_{\mathrm{eff}}(r)}{T^l_{\mathrm{i}}(r) + Z^l_{\mathrm{eff}}(r) T^l_{\mathrm{e}}(r)}} \ . \tag{23}$$

Each up-stream Langmuir probe data-set was updated with the profile of the effective charge state Z_{eff} and the effective mass m_{eff} from the simulation to which the $n_{\mathrm{e,MPM}}$ profile was compared before. Hence, an $n_{\mathrm{e,EMC3}}$ profile which is coinciding to the profile of the Langmuir probe measurement $n_{\mathrm{e,MPM}}$ is also leading to a convergence of the Z_{eff} and m_{eff} profiles (see figure 8). MPM Langmuir probe measurements were not able to separate the electron temperature T_{e} from the ion temperature T_{i} of the plasma. Hence, T_{e} and T_{i} are taken from EMC3-EIRENE.
From now on, $\Lambda^{l_{\mathrm{end}}}$ will refer to the simulation setup with the factor ε^l which is closest to 1. Figure 9 shows in plot (a) the relative change of ε^l calculated by equation (23). The relative change for $n_{\mathrm{e,MPM}}$ (shown in (b) of figure 9), Z_{eff} and m_{eff} (both shown in (c) of figure 9) drops below 1% for an input density of 2.793×10^{18} m^{-3} (used in

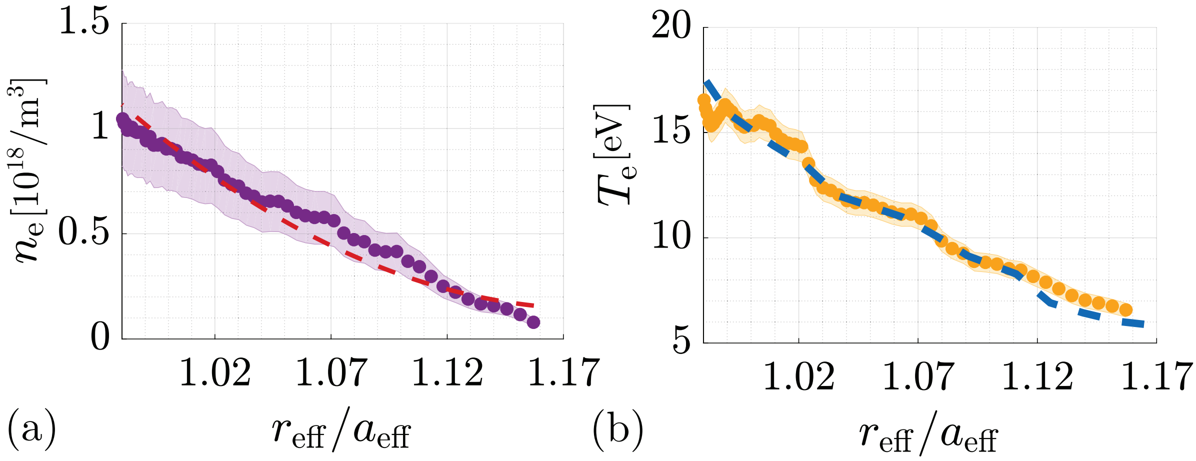

Figure 10: Final comparison between EMC3-EIRENE simulation (dashed) and $Z_{\mathrm{eff}}^{l_{\mathrm{end}}}$ adjusted manipulator Langmuir probe measurements (dots). Plot (a) shows n_{e}, (b) shows T_{e}. Simulation parameters used from plasma scenario $\Lambda^{l_{\mathrm{end}}}$.

the last iterative step). Figure 7 (a) and (b) shows up- and down-stream Z_{eff} profiles of the last iterative step using the simulation setup $\Lambda^{l_{\mathrm{end}}}$. As the relative deviation of Z_{eff} and m_{eff} for the up-stream region converges to a value below 1%, an overall agreement between the measurement and simulation is shown as the final result in figure 10. Shown measured density profiles are refined by 16% to more correct and consistent profiles. In section 3 simulation Λ provided an overall agreement to the Langmuir probe measurements at the up- and down-stream location. Now, the simulation $\Lambda^{l_{\mathrm{end}}}$ shows again an overall agreement for the up-stream measurement location including a more reasonable estimate for up-stream Z_{eff} and m_{eff} profiles. Worth to emphasize is the convergence of the estimated Z_{eff} and m_{eff} profiles in the iterative process which directly affect Langmuir probe data processing. The resulting final profiles of the MPM measurement (see figure 10) lie at the bottom edge of the uncertainties (refinement of 12%) of the unrefined n_{e} profiles shown in figure 4 (matched by EMC3-EIRENE using Λ). The initial assumption of Z_{eff} and m_{eff} to be equal to 1 is proven to be plausible. Hence, a reinterpretation process of the Langmuir probe measurements shown in this paper appears to be irrelevant at first glance. However, the shown Langmuir probe measurements were used as reference points to consistently assess missing Z_{eff} and m_{eff} profiles. Assessed Z_{eff} profiles lie reasonably close (30% in a maximum difference) to the made assumptions ($Z_{\mathrm{eff}} = 1$). We infer that the considered discharges reflect discharges with a small contamination of impurities. A relative low radiated power was measured for the shown plasma scenario Λ (see figure 2). This measure is directly linked to the amount of impurities which soil the plasma scenario, and gives a plausible explanation for the minor impact of the reinterpretation process.

Additionally, each simulation setup shown in figure 10 was accompanied by a scan over the diffusion coefficient and the radiated Power $P_{\mathrm{rad}}^{\mathrm{SOL}}$. Free input parameters like $D_{\perp}$ underlie an initial guess. A sensitivity study for $n_{\mathrm{e,EMC3}}$ concerning $D_{\perp}$ and $P_{\mathrm{rad}}^{\mathrm{SOL}}$

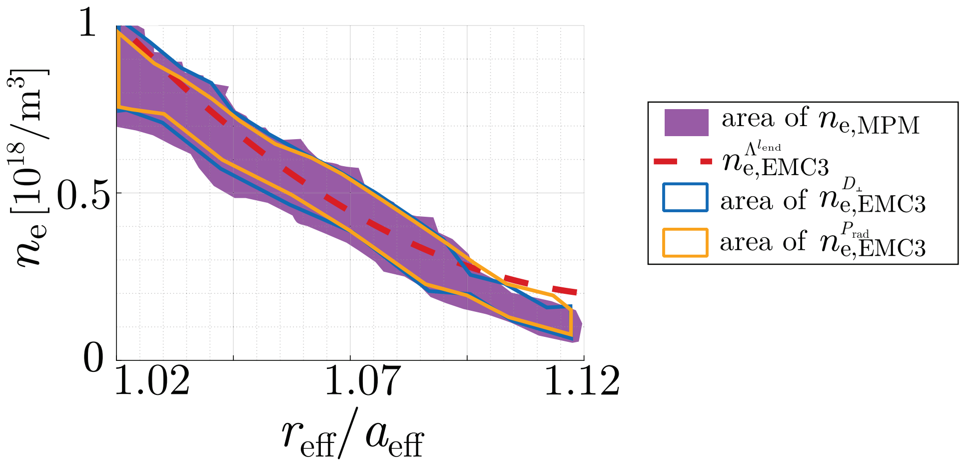

Figure 11: Overview of the influence of a variation over $D_\perp$ and $P_{\mathrm{rad}}^{\mathrm{SOL}}$ on $n_{\mathrm{e,EMC3}}$, plotted in translucent areas which entail the simulation results for $n_{\mathrm{e,EMC3}}^{\mathrm{D}}$ and $n_{\mathrm{e,EMC3}}^{\mathrm{P_{rad}^{SOL}}}$. Plotted in comparison to the magenta shaded area of $n_{\mathrm{e,MPM}}$ and $n_{\mathrm{e,EMC3}}^{\Lambda^{l_{\mathrm{end}}}}$ as a guide to the eye.

(free input parameters) is performed, to cover the influence of these free simulation parameters. The diffusion coefficient $D_\perp$ is chosen in $D_\perp \in [0.4,\ 0.5,\ 0.6]\ \frac{\mathrm{m}^2}{s}$ and $P_{\mathrm{rad}}^{\mathrm{SOL}}$ is chosen in $P_{\mathrm{rad}}^{\mathrm{SOL}} = [60,\ 120,\ 180]$ kW for each iterative step. The variation of $D_\perp$ and $P_{\mathrm{rad}}^{\mathrm{SOL}}$ resulted in both cases for each iterative step in profiles which again show a consistency between $n_{\mathrm{e,EMC3}}$ and $n_{\mathrm{e,MPM}}$. The resulting change of $n_{\mathrm{e,EMC3}}$ is observable in the enclosed area of $n_{\mathrm{e,EMC3}}^{D_\perp}$ and $n_{\mathrm{e,EMC3}}^{P_{\mathrm{rad}}}$ of figure 11. The overlap of the simulated $n_{\mathrm{e,EMC3}}$ and measured $n_{\mathrm{e,MPM}}$ (with error bars) remains high, thus the consistency between $n_{\mathrm{e,EMC3}}$ and $n_{\mathrm{e,MPM}}$ is preserved concerning the variation of $D_\perp$ and $P_{\mathrm{rad}}^{\mathrm{SOL}}$.

5. Conclusion

Interpretative EMC3-EIRENE simulations are used to assess plasma parameters which were not directly accessible by any diagnostic available on W7-X in OP1.1. Inferred spatial Z_{eff} and m_{eff} profiles were identified as further sensitive input information for the data processing of several W7-X diagnostics, especially Langmuir probes, as these diagnostics rely on the knowledge of radial Z_{eff} profiles at their measurement position. An iterative reprocessing of the Langmuir probe data was performed in comparison to EMC3-EIRENE simulations. This finally led to a fully 3D resolved edge plasma simulation which lies in overall agreement with the available up- and down-stream measurements, including Z_{eff} consistent with measured radiative power losses.
We conclude that more generally in 3D magnetic configurations, edge plasma diagnostics, which rely on assumptions over spatial plasma parameter distributions such as Z_{eff} can profit from this complementary "numerical" diagnostic.
Further model refinements, in particular in the trace impurity ion fluid model and

comparison of simulations to further W7-X diagnostics, are steps which have to be taken in the future, in particular when oxygen, with its (hitherto neglected) accidental charge exchange resonance, remains a relevant plasma impurity in W7-X discharges. Furthermore, oxygen impurities will have an higher impact on Z_{eff} and m_{eff} profiles than carbon as single impurity. The impact of the reinterpretation process will become more pronounced. Discharges of OP 1.2 in a divertor configuration will be evaluated regarding to this impact.

Acknowledgments

We are thankful for the valuable discussions with Dirk Reiser, Felix Reimold and Glen Wurden. The authors gratefully acknowledge the computing time granted by the JARA-HPC Vergabegremium and VSR commission on the supercomputer JURECA at Forschungszentrum Jülich. This work has been carried out within the framework of the EUROfusion Consortium and has received funding from the Euratom research and training programme 2014-2018 under grant agreement no. 633053. The views and opinions expressed here in do not necessarily reflect those of the European Commission.

Appendix. Discussion of the impurity model.

The parallel impurity force balance (species/charge state α) in EMC3 reads ($\hat{\mathbf{e}}_{\parallel} \cdot \boldsymbol{\nabla} = \nabla_{\parallel},\ p_\alpha = n_\alpha T_\alpha$)

$$0 = -\hat{\mathbf{e}}_{\parallel} \cdot \boldsymbol{\nabla} p_\alpha + Z_\alpha n_\alpha e E_{\parallel} + \frac{\mu_{\alpha i}}{\tau_{\alpha i}} n_\alpha (u_{i\parallel} - u_{\alpha\parallel}) + \alpha_{\alpha e} n_\alpha \nabla_{\parallel} T_e + + \beta_{\alpha i} n_\alpha \nabla_{\parallel} T_i + S_{\mathrm{m}\alpha}\ . \quad (24)$$

with the pressure gradient force, electric force, frictional force, electron and ion thermal force, respectively. The momentum sources $S_{\mathrm{m}\alpha}$ due to ionisation, recombination with neighbouring charge states as well as due to interaction of impurity ion α with any of the kinetically treated species in EIRENE is neglected: $S_{\mathrm{m}\alpha} = 0$. μ is the reduced mass, and the collision times τ and electron-ion thermal force coefficients $\alpha_{\alpha e} = 0.71 Z_\alpha^2$ are again taken from Braginskii [5]. A low impurity concentration limit ($n_\alpha \ll n_i$) expression for the ion-ion thermal force coefficient $\beta_{\alpha i}$ is used, which was originally derived by S. Chapman (1958), and later frequently employed as approximation in tokamak and stellarator edge transport models [24]:

$$\beta_{\alpha i} = -3\ \frac{1 - \tilde{\mu} - 5\sqrt{2}(Z_\alpha/Z_i)^2\ (1.1\tilde{\mu}^{5/2} - 0.35\tilde{\mu}^{3/2})}{2.6 - 2\tilde{\mu} + 5.4\tilde{\mu}^2}, \quad \tilde{\mu} = \frac{m_\alpha}{m_\alpha + m_{\mathrm{i}}} \quad . \quad (25)$$

As usual, instead of the Poisson equation the common "plasma approximation" is made to express the parallel electric field in (24) via the (here strongly reduced) electron momentum balance (neglecting all terms containing the electron mass):

$$eE_{\parallel} = -\frac{1}{n_e} \nabla_{\parallel} p_e - \alpha_{ie} \nabla_{\parallel} T_e \quad (26)$$

Inserting this into (24) provides the explicit expression for the parallel impurity ion flow velocity $u_{\alpha\|}$:

$$u_{\alpha\|} = u_{i\|} + \frac{\tau_{\alpha i}}{\mu_{\alpha i}}\left[(\beta_{\alpha i}-1)\nabla_{\|}T_i - \frac{Z_\alpha}{n_e}\nabla_{\|}p_e + (\alpha_{\alpha e} - Z_\alpha \alpha_{ie})\nabla_{\|}T_e\right] + \frac{\tau_{\alpha i}}{\mu_{\alpha i} n_\alpha} T_i \nabla_{\|} n_\alpha \quad . \tag{27}$$

Denoting the first part on the r.h.s. by $U_{\alpha\|}$ and introducing the (binary) diffusion coefficient due to friction between main ions and impurity ions $D^f_{\alpha\|} = \frac{\tau_{\alpha i}T_i}{\mu_{\alpha i}}$ a diffusion - advection expression for the parallel impurity ion flux Γ_α results:

$$\Gamma_{\alpha\|} = n_\alpha u_{\alpha\|} = n_\alpha U_{\alpha\|} - D^f_{\alpha\|}\nabla_{\|}n_\alpha \quad . \tag{28}$$

Inserting (28) into (1) leads to an impurity continuity equation:

$$\boldsymbol{\nabla}\cdot\left[n_\alpha U_{\alpha\|}\hat{\mathbf{e}}_{\|} - D^f_{\alpha\|}\nabla_{\|}n_\alpha - D_\perp \boldsymbol{\nabla}_\perp n_\alpha\right] = S_\alpha \quad . \tag{29}$$

In addition, $T_\alpha = T_{\mathrm{i}}$ is assumed for all impurity species α, and each charge state is treated as a separate fluid. The (particle) source term S_α provides the coupling between neighboring charge states due to ionisation and recombination, and, for the single charged impurity ion, the ionisation rate from neutral impurity atoms. The latter are launched, mono-energetically, from target surfaces with a given sputtering rate, and then simply exponentially decayed due to ionisation into the plasma. Again the identity preserving Lagrangian scheme mentioned above is utilized for the transfer from neutral to ionised impurities (rather than re-sampling from volumetric neutral impurity sources), distinct from the current re-sampling coupling procedure for neutrals and molecules treated fully kinetically by EIRENE. There is, in principle no limitation on the number of impurity species (within the trace impurity transport model), as long as the concentration of the impurities is limited by the assumption $n_\alpha \ll n_{\mathrm{e}}$ and inter-impurity effects other than those in the source terms can be neglected.

Equation (29) for n_α is then coupled to the electron energy balance equation (3) of the main plasma, via the cooling term $S_{e,cool}$. A detailed discussion of impurity radiation and the resulting cooling effect on the energy balance equation (3) is given in [25]. Within an iterative process a self-consistent solution for the mentioned plasma parameters, $n, T_\alpha, u_\|, n_\alpha$ and $S_{\mathrm{e,cool}}$ is obtained. Impurities return back into the edge region with the same charge as they entered the core region, i.e. the net flux across the core boundary is set to zero for each charge state individually. Furthermore: a toroidally and poloidally homogeneous density is enforced for each charge state, on that core boundary. A radial decay length of 4 cm for n and T_α is implemented as boundary condition for the outer radial first wall boundary throughout this work. Impurities which reach the target are absorbed.

References

[1] T. Klinger et al. Performance and properties of the first plasmas of Wendelstein 7-X. *Plasma Physics and Controlled Fusion*, 59(1):014018, 2017.

[2] C.D. Beidler et al. Physics and engineering design for Wendelstein 7-X. *Fusion Technology*, 17(1):148–168, 1990.

[3] Y. Feng. 3D fluid modelling of the edge plasma by means of a Monte Carlo technique. *Journal of Nuclear Materials*, 266-269:812–818, 1999.

[4] D. Reiter. The EIRENE and B2-EIRENE Codes. *Fusion Science and Technology*, 47:172–186, 2005.

[5] S. I. Braginskii. Transport Processes in a Plasma. *Reviews of Plasma Physics*, 1:205, 1965.

[6] A. Diggs and S. Balachandar. Modeling and simulation challenges in eulerian-lagrangian computations of multiphase flows. *AIP Conference Proceedings*, 1793(1):150008, 2017.

[7] T. S. Pedersen et al. Plans for the first plasma operation of Wendelstein 7-X. *Nuclear Fusion*, 55(12):126001, 2015.

[8] R. Wolf et al. Major results from the first plasma campaign of the Wendelstein 7-X stellarator. 57, 06 2017.

[9] M. Krychowiak et al. Overview of diagnostic performance and results for the first operation phase in Wendelstein 7-X. *Review of Scientific Instruments*, 87(11):11D304, 2016.

[10] P. Drews et al. Measurement of the plasma edge profiles using the combined probe on W7-X. *Nuclear Fusion*, 57(12):126020, 2017.

[11] D. Nicolai et al. A multi-purpose manipulator system for W7-X as user facility for plasma edge investigation. *Fusion Engineering and Design*, 123(Supplement C):960 – 964, 2017. Proceedings of the 29th Symposium on Fusion Technology (SOFT-29) Prague, Czech Republic, September 5-9, 2016.

[12] G. Satheeswaran et al. A PCS7-based control and safety system for operation of the W7-X Multi-Purpose Manipulator facility. *Fusion Engineering and Design*, 123(Supplement C):699 – 702, 2017. Proceedings of the 29th Symposium on Fusion Technology (SOFT-29) Prague, Czech Republic, September 5-9, 2016.

[13] H. Meister et al. An integrated system to measure the effective charge of fusion plasmas in the ASDEX Upgrade tokamak. *Review of Scientific Instruments*, 74(11):4625–4633, 2003.

[14] Y. Feng et al. 3D edge modeling and island divertor physics. *Contributions to Plasma Physics*, 44 (1-3):57–69, 2004.

[15] D. Reiter. Randschicht-Konfiguration von Tokamaks. Entwicklung und Anwendung stochastischer Modelle zur Beschreibung des Neutralgastransports. 0366-0885(1947), 1984.

[16] M. Rack et al. A fluid-kinetic approach for 3D plasma edge transport in He plasma. *Nuclear Fusion*, 57 (5):056011, 2017.

[17] M. Hirsch et al. Confinement in Wendelstein 7-X limiter plasmas. *Nuclear Fusion*, 57(8):086010, 2017.

[18] H. Niemann et al. Power loads in the limiter phase of Wendelstein 7-X. 4:5, 2016.

[19] F. Effenberg. Numerical investigation of plasma edge transport and limiter heat fluxes in Wendelstein 7-X startup plasmas with EMC3-EIRENE. *Nuclear Fusion*, 57, 2017.

[20] P.C. Stangeby. The plasma boundary of magnetic fusion devices. ISBN 0 7503 0559 2, 2000.

[21] M. Z. Tokar'. Fluid approximation of the bohm criterium for plasmas of several ion species. *Contributions to Plasma Physics*, 34(23):139–144.

[22] Y. Igitkhanov. Modelling of multi-component plasmas for tokes. *KIT Scientific Reports*, 7564:ISSN 1869–9669.

[23] H-B Valentini et al. Boundary value problems for multi-component plasmas and a generalized bohm criterion. *Journal of Physics D: Applied Physics*, 29(5):1175, 1996.

[24] J. Neuhauser. Modelling of impurity flow in the tokamak scrape-off layer. *Nuclear Fusion*, 24:39, 1984.

[25] H. Frerichs. Three-dimensional plasma transport in open chaotic magnetic fiels. A computational assessment for tokamak edge layers. *Technical Report*, Jül(4321), 2010.

Jül-4414 • Juli 2018
ISSN 0944-2952

Mitglied der Helmholtz-Gemeinschaft

JÜLICH
Forschungszentrum